

A lattice Boltzmann method for Biot's consolidation model of linear poroelasticity

Stephan B. Lunowa^{a,*}, Barbara Wohlmuth^a

^a*Technical University of Munich, School of Computation, Information and Technology, Department of Mathematics, Boltzmannstraße 3, D-85748, Garching, Germany*

Abstract

Biot's consolidation model is a classical model for the evolution of deformable porous media saturated by a fluid and has various interdisciplinary applications. While numerical solution methods to solve poroelasticity by typical schemes such as finite differences, finite volumes or finite elements have been intensely studied, lattice Boltzmann methods for poroelasticity have not been developed yet. In this work, we propose a novel semi-implicit coupling of lattice Boltzmann methods to solve Biot's consolidation model in two dimensions. To this end, we use a single-relaxation-time lattice Boltzmann method for reaction-diffusion equations to solve the Darcy flow and combine it with a recent pseudo-time multi-relaxation-time lattice Boltzmann scheme for quasi-static linear elasticity by Boolakee, Geier and De Lorenzis (2023) [1]. The numerical results demonstrate that naive coupling schemes lead to instabilities when the poroelastic system is strongly coupled. However, the newly developed centered coupling scheme using fully explicit and semi-implicit contributions is stable and accurate in all considered cases, even for the Biot-Willis coefficient being one. Furthermore, the numerical results for Terzaghi's consolidation problem and a two-dimensional extension thereof highlight that the scheme is even able to capture discontinuous solutions arising from instantaneous loading.

Keywords: Lattice Boltzmann method, Biot's consolidation model, Linear poroelasticity
2020 MSC: 35Q86, 65M75, 74F10

1. Introduction

The evolution of deformable porous media saturated by a fluid is subject to long-lasting scientific investigations due to its various interdisciplinary applications ranging from geological CO₂ storage [2] and geothermal energy [3], over material design for nano-composites [4] and concrete [5], to the function of biological tissue [6] such as the optic nerve [7] and heart dynamics [8]. The theoretical origin dates back to 1923, when Terzaghi developed a description of one-dimensional consolidation [9]. In the subsequent decades, the theory was extended by Biot [10–13] leading to the nowadays called Biot's consolidation model. It describes the two-phase solid-fluid systems based on a linearly elastic, porous solid skeleton that undergoes small deformations, while the fluid flow induced by the deformation of the solid is governed by Darcy's law. For a general introduction to linear and non-linear poroelasticity, we refer the interested reader to [14, 15].

Since analytical solutions to the model are very scarce, there is a large number of numerical methods for solving the coupled system. Starting from classical finite difference methods [16–18] and finite element methods [19, 20], more advanced schemes were developed to improve the approximation of stress and flux and allow for strongly heterogeneous material parameters. This has led to multiple finite volume methods [21–23], and a large class of tailored finite element methods using, e.g., discontinuous Galerkin [24, 25], mixed finite elements [26, 27], or enriched

*Corresponding author

Email addresses: stephan.lunowa@tum.de (Stephan B. Lunowa), wohlmuth@tum.de (Barbara Wohlmuth)

URL: orcid.org/0000-0002-5214-7245 (Stephan B. Lunowa), orcid.org/0000-0001-6908-6015 (Barbara Wohlmuth)

finite elements [28]. Furthermore, these methods can account for local mass conservation, avoid locking effects and suppress non-physical pressure oscillations.

A substantially different numerical approach are lattice Boltzmann methods (LBMs), which were originally developed for the simulation of fluid dynamics [29, 30]. In contrast to the above mentioned methods, which rely on the approximation of the macroscopic equations, the LBM is based on a mesoscopic description of statistical physics for gas particle dynamics, i.e., the discretization of the Boltzmann equation in physical and velocity space. While the single-relaxation-time collision operator [31] is most popular due to its simplicity, variants based on multiple relaxation times [32] and cumulants [33] are used for more complex problems to improve accuracy, stability and the number of represented physical parameters. For a detailed introduction to LBM, we refer to [34, 35]. A major advantage of LBM is the simple algorithmic structure and the straightforward parallelization, especially on GPUs, which make the method well suited for modern, massively parallel and hybrid computing architectures [36, 37].

Nowadays, various LBMs exist for most of the partial differential equations encountered in practice. In particular, LBMs were quickly adapted for advection-diffusion-reaction equations which have a similar structure as the Navier-Stokes equations. This was originally recognized for pure diffusion in [38], for advection-diffusion problems in [39] and for diffusion-reaction problems in [40]. Based on these works, the method has been extended in several ways. Anisotropic diffusion and dispersion was included by a direction-dependent relaxation in [41] and using a multiple-relaxation-time (MRT) scheme in [42]. The full advection-diffusion-reaction equation was considered in [43] using a source-correction scheme involving the temporal derivative, while a simpler moment update was proposed in [44]. Furthermore, nonlinear coefficients were incorporated in [45] and combined with a MRT scheme for anisotropy in [46]. We refer to [47] for a detailed analysis of LBM for nonlinear and anisotropic advection-diffusion-reaction equations.

Concerning linear elasticity, the first LBM was introduced in [48] using two wave equations of the same speed describing the motion of longitudinal and transverse displacements. This approach was adopted in [49] using extended velocity sets in 2D and 3D combined with finite difference schemes and flux limiters to avoid spurious oscillations. Furthermore, arbitrary Poisson's ratios, and thus different wave speeds, were achieved by an extension developed in [50] for hypoelastic materials and in [51] for linear materials. Several boundary conditions to this method were developed in [51, 52]. Another approach is discussed in [53], where anti-plane shear deformation is assumed to simplify the equations into a scalar wave equation, that is subsequently solved by LBM. An extension to two wave equations describing dilation and rotation in 2D is presented in [54]. There, the two equations are solved by two separate LBMs, which are coupled via finite difference schemes. Recently, a vectorial LBM has been proposed in [55] for linear elastodynamics in two-dimensional domains with periodic or Dirichlet boundary.

While all these methods solve dynamic elasticity, the approximation of quasi-static elasticity by LBM is more intricate. LBMs are essentially explicit schemes in time, and hence not directly applicable to elliptic equations. To circumvent this, the addition of a time-dependent damping term was proposed in [56], which leads to an iterative LBM that solves the quasi-static equation when approaching the steady-state. In particular, the method in [56] combines a vectorial LBM for the components of the displacement with a finite difference approximation of the divergence. Using the same pseudo-time approach, quasi-static linear elasticity in 2D has been solved in [1] using a MRT LBM on a reduced velocity stencil. While originally posed as an periodic problem, the treatment of Dirichlet and Neumann boundary conditions is discussed in [57].

However, to the best of the authors' knowledge, there have not been developed any LBMs for solving poroelasticity yet. In this work, we propose a novel coupled LBM to solve Biot's consolidation model in two dimensions. To this end, we use the classical LBM for reaction-diffusion equations [44] for the Darcy flow and combine it with the recent pseudo-time LBM for quasi-static linear elasticity [1]. We demonstrate that a naively coupled LBMs lead to instabilities for a strongly coupled problem (Biot-Willis coefficient close to one), while a coupling scheme using fully explicit and semi-implicit contributions is stable and accurate for all Biot-Willis coefficients. The numerical results for Terzaghi's consolidation problem highlight that the scheme is even able to capture solutions with discontinuities arising from instantaneous loading.

The outline of this paper is as follows. The governing equations of Biot's consolidation model are presented in Section 2. Next, we introduce the LBMs for flow and elasticity in Section 3, discussing in detail the coupling and used initial and boundary conditions. In Section 4, we present numerical results for a problem with a manufactured solution, for Terzaghi's consolidation problem as well as for an two-dimensional extension of the latter. Finally, Section 5 summarizes the main conclusions.

2. Governing equations

In the following two subsections, we first present the system of equations representing Biot's consolidation model in dimensional form and subsequently derive the dimensionless formulation, which will be used in the LBM.

2.1. Biot's consolidation model

We consider Biot's model of consolidation for a linearly elastic and porous solid, which is saturated by a slightly compressible viscous fluid [11, 13–15]. For given final time $t_f \in (0, \infty)$ and a simply connected, Lipschitz-bounded domain $\mathcal{D} \in \mathbb{R}^d$, we define the time-space cylinder $\mathcal{Q} = (0, t_f) \times \mathcal{D}$. Note that we discuss in this section the general model with dimension $d \in \{1, 2, 3\}$, whereas we restrict ourselves to $d = 2$ thereafter for the LBM. Furthermore, the displacement and stress of the solid are denoted by $\boldsymbol{\eta} : \mathcal{Q} \rightarrow \mathbb{R}^d$ and $\boldsymbol{\sigma} : \mathcal{Q} \rightarrow \mathbb{R}^{d \times d}$, respectively, while the fluid pressure and Darcy velocity are denoted by $p : \mathcal{Q} \rightarrow \mathbb{R}$ and $\mathbf{u} : \mathcal{Q} \rightarrow \mathbb{R}^d$, respectively. Assuming an isotropic material, the system of partial differential equations reads

$$-\nabla \cdot \boldsymbol{\sigma} + \alpha \nabla p = \mathbf{f} \quad \text{in } \mathcal{Q}, \quad (1)$$

$$\boldsymbol{\sigma} = \lambda(\nabla \cdot \boldsymbol{\eta})\mathbf{I} + \mu(\nabla \boldsymbol{\eta} + \nabla \boldsymbol{\eta}^\top) \quad \text{in } \mathcal{Q}, \quad (2)$$

$$\partial_t(c_0 p + \alpha \nabla \cdot \boldsymbol{\eta}) + \nabla \cdot \mathbf{u} = s \quad \text{in } \mathcal{Q}, \quad (3)$$

$$\mathbf{u} = -\kappa(\nabla p - \mathbf{g}) \quad \text{in } \mathcal{Q}. \quad (4)$$

Here, the first two equations describe the quasi-static force balance in the deformed solid, while the last two equations describe the diffusive Darcy flow of the fluid due to the deformation. The so-called Biot–Willis parameter $\alpha \in (0, 1]$ represents the interaction strength between solid and fluid ranging from no coupling in the limit $\alpha \rightarrow 0$ to strong coupling for α close to 1. Moreover, λ and μ denote the first and second Lamé coefficients of the solid, c_0 is the specific storage coefficient and κ represents the viscosity-reduced permeability. Finally, the right-hand side \mathbf{f} and \mathbf{g} are given volume forces for solid and fluid, respectively, while s is a volumetric fluid source or sink.

The system has to be closed by appropriate initial and boundary conditions for the primal unknowns $\boldsymbol{\eta}$ and p . We omit the details here and will specify the conditions used for the numerical examples in Section 4 and their LBM implementations in Section 3.5. Note that a derivation of this model by homogenization can be found in [58], while a rigorous mathematical analysis of this problem is presented in [59].

2.2. Dimensionless system of equations

For the dimensionless formulation, we introduce a characteristic length L , time T , scalar displacement H and pressure $P = c_0^{-1}$. With this reference system, the dimensionless quantities are defined by

$$\hat{\mathbf{x}} = \frac{\mathbf{x}}{L}, \quad \hat{t} = \frac{t}{T}, \quad \hat{\boldsymbol{\eta}} = \frac{\boldsymbol{\eta}}{H}, \quad \hat{\boldsymbol{\sigma}} = \frac{c_0 L \boldsymbol{\sigma}}{H}, \quad \hat{p} = c_0 p, \quad \hat{\mathbf{u}} = \frac{T \mathbf{u}}{L},$$

while the dimensionless derivatives satisfy $\hat{\nabla} = L \nabla$ and $\partial_{\hat{t}} = T \partial_t$. Accordingly, the scaled time-space cylinder is given by $\hat{\mathcal{Q}} = \{(\hat{t}, \hat{\mathbf{x}}) \mid (t, \mathbf{x}) \in \mathcal{Q}\}$. Inserting the dimensionless quantities into the Biot system Eqs. (1) to (4) yields

$$-\hat{\nabla} \cdot \hat{\boldsymbol{\sigma}} + \varepsilon \alpha \hat{\nabla} \hat{p} = \varepsilon \hat{\mathbf{f}} \quad \text{in } \hat{\mathcal{Q}}, \quad (5)$$

$$\hat{\boldsymbol{\sigma}} = \hat{\lambda}(\hat{\nabla} \cdot \hat{\boldsymbol{\eta}})\mathbf{I} + \hat{\mu}(\hat{\nabla} \hat{\boldsymbol{\eta}} + \hat{\nabla} \hat{\boldsymbol{\eta}}^\top) \quad \text{in } \hat{\mathcal{Q}}, \quad (6)$$

$$\partial_{\hat{t}} \left(\hat{p} + \frac{\alpha}{\varepsilon} \hat{\nabla} \cdot \hat{\boldsymbol{\eta}} \right) + \hat{\nabla} \cdot \hat{\mathbf{u}} = \hat{s} \quad \text{in } \hat{\mathcal{Q}}, \quad (7)$$

$$\hat{\mathbf{u}} = -\hat{\kappa}(\hat{\nabla} \hat{p} - \hat{\mathbf{g}}) \quad \text{in } \hat{\mathcal{Q}}, \quad (8)$$

where the dimensionless parameters are

$$\varepsilon = \frac{L}{H}, \quad \hat{\lambda} = c_0 \lambda, \quad \hat{\mu} = c_0 \mu, \quad \hat{\kappa} = \frac{T \kappa}{c_0 L^2},$$

and the dimensionless forces and source are given by

$$\hat{\mathbf{f}} = c_0 L \mathbf{f}, \quad \hat{\mathbf{g}} = c_0 L \mathbf{g}, \quad \hat{s} = T s.$$

In the following, we drop the hats for readability.

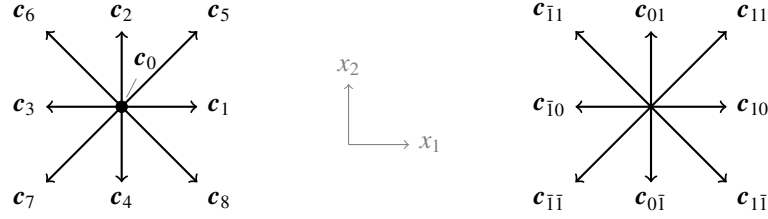


Figure 1: D2Q9 velocity set c_i with linear indices (left) and D2Q8 velocity set c_{ij} with 2D Miller indices, i.e., $\bar{1} = -1$ (right).

Table 1: Discrete velocities c_i and weights w_i with linear and 2D Miller indices, i.e., $\bar{1} = -1$.

Linear index	0	1	2	3	4	5	6	7	8
Miller index	00	10	01	$\bar{1}0$	$0\bar{1}$	11	$\bar{1}\bar{1}$	$\bar{1}1$	$1\bar{1}$
Velocity	$\begin{pmatrix} 0 \\ 0 \end{pmatrix}$	$\begin{pmatrix} 1 \\ 0 \end{pmatrix}$	$\begin{pmatrix} 0 \\ 1 \end{pmatrix}$	$\begin{pmatrix} -1 \\ 0 \end{pmatrix}$	$\begin{pmatrix} 0 \\ -1 \end{pmatrix}$	$\begin{pmatrix} 1 \\ 1 \end{pmatrix}$	$\begin{pmatrix} -1 \\ -1 \end{pmatrix}$	$\begin{pmatrix} -1 \\ 1 \end{pmatrix}$	$\begin{pmatrix} 1 \\ -1 \end{pmatrix}$
Weight	4/9	1/9	1/9	1/9	1/9	1/36	1/36	1/36	1/36

3. The lattice Boltzmann method for Biot's consolidation model

In this section, we propose the LBM for Biot's consolidation model by coupling LBM for the diffusive fluid flow [44] with LBM for two-dimensional linear elasticity [1, 57]. To this end, we introduce notation conventions and basic definitions first and subsequently present the separate LBMs for diffusive flow and elasticity. Then, we discuss the coupling of the two methods and finally elaborate on the LBM implementation of the used initial and boundary conditions.

3.1. Notation and definitions for lattice Boltzmann methods

In the following, we summarize all basics of LBM necessary for this work, for a detailed introduction we refer to [34, 35]. The fundamental principle of LBM is the discretization of the Boltzmann equation in physical and velocity space. For this purpose, the main variable is the distribution function f , which denotes the probability of material particles at time t and position \mathbf{x} to have the velocity \mathbf{c} . The velocity space is discretized using a finite set of velocities c_i and corresponding weights w_i , such that $f_i(t, \mathbf{x}) = f(t, \mathbf{x}, c_i)$. These sets are typically derived based on the required mass, momentum and energy conservation using a Hermite series expansion. Typically, the velocity sets are denoted by $DdQq$, where d is the dimension and q the number of discrete velocities. For the two-dimensional LBMs presented in the following, we utilize the classical D2Q9 velocity set as well as a reduced D2Q8 velocity set without rest velocity $c_0 = \mathbf{0}$, see Fig. 1 and Table 1.

Additionally, the two-dimensional domain \mathcal{D} is discretized by a uniform lattice of width Δx , while the time interval $(0, t_f)$ is discretized by a uniform time step $\Delta t = t_f/N_T$ with $N_T \in \mathbb{N}$. This leads to a discrete lattice speed of sound $c_s = \Delta x/(\sqrt{3}\Delta t)$. Altogether, the general lattice Boltzmann equation then reads

$$f_i(t + \Delta t, \mathbf{x} + \Delta t c_i) - f_i(t, \mathbf{x}) = \Delta t \Omega_i(t, \mathbf{x}), \quad (9)$$

where the lefthand side represents an advection along the discrete velocity c_i , the so-called streaming step, whereas the righthand side term, called collision operator contains all interactions such as relaxation to equilibrium due to particle collision as well as external forces and sources. Note that the lattice Boltzmann equation can be split in two parts: the collision step

$$f_i^*(t, \mathbf{x}) = f_i(t, \mathbf{x}) + \Delta t \Omega_i(t, \mathbf{x}), \quad (10)$$

which is local, and the streaming step

$$f_i(t + \Delta t, \mathbf{x} + \Delta t c_i) = f_i^*(t, \mathbf{x}), \quad (11)$$

which moves each distribution function one lattice node further in their velocity direction. This is the fundamental reason for the algorithmic simplicity and for the straightforward and well-scaling parallelization.

Even in the absence of external interactions, the collision operator is very complicated as it involves all types of microscopic particle interactions. However, the most simple approximation, which ensures mass and momentum conservation, is given by the Bhatnagar–Gross–Krook collision operator [31]

$$\Omega_i = -\omega(f_i - f_i^{\text{eq}}), \quad (12)$$

where $\omega > 0$ is the relaxation rate towards the equilibrium state f_i^{eq} that depends on the moments of all distribution functions f_j according to the equation of interest, e.g., on density $\rho = \sum_i f_i$ and momentum $\rho \mathbf{u} = \sum_i f_i \mathbf{c}_i$ in case of the Navier–Stokes equations. Note that here and in the following, the arguments (t, \mathbf{x}) are omitted whenever the meaning is unambiguous. The Bhatnagar–Gross–Krook collision operator will be used below for the diffusive fluid flow. In this application, the relaxation rate is directly related to the diffusion coefficient.

In contrast to this single-relaxation-time scheme, multiple-relaxation-time (MRT) collision operators allow for a larger number of free parameters, increased stability and higher accuracy. This is necessary to formulate a LBM for linear elasticity. For MRT schemes, the distribution functions are transformed into linear independent moments, which are individually relaxed at different rates and then transformed back to the distributions [32]. Denoting the vector of the distribution functions for all discrete velocities by $\mathbf{f} = (f_0, \dots, f_8)^\top$, the transformation into moments can be described by multiplication by an invertible matrix \mathbf{M} . Analogously, we represent the individual relaxation rates as a diagonal matrix ω and the equilibrium moment vector by \mathbf{m}^{eq} . The vector of MRT collision operators for all discrete velocities is then given by

$$\mathbf{\Omega} = -\mathbf{M}^{-1}\omega(\mathbf{M}\mathbf{f} - \mathbf{m}^{\text{eq}}). \quad (13)$$

The specific moments and relaxation rates depend again on the parameters of the considered equations. More details will be given below during the discussion of LBM for linear elasticity. Finally, note that the Bhatnagar–Gross–Krook collision operator is a special case of the MRT one when $\omega = \omega \mathbf{I}$ is chosen.

3.2. The lattice Boltzmann method for diffusive fluid flow

In the following, we present the required steps for the LBM solving the diffusive fluid flow Eqs. (7) and (8). Combining these equations and reordering the terms, we obtain the diffusion-reaction equation

$$\partial_t p - \kappa \Delta p = s_{\text{eff}} = s - \kappa \nabla \cdot \mathbf{g} - \frac{\alpha}{\varepsilon} \partial_t \nabla \cdot \boldsymbol{\eta} \quad \text{in } \mathcal{Q}. \quad (14)$$

Subsequently, the LBM for the diffusion-reaction equation proposed in [44] is discussed, while the detailed computation of the effective source term s_{eff} is deferred to Section 3.4. Following the presentation in [34, Chpt. 8], this LBM is based on the single-relaxation-time scheme Eqs. (9) and (12) and uses the D2Q9 velocity set. Denoting the distribution functions for the pressure by f_i with linear index $i \in \{0, 1, \dots, 8\}$, the pressure p is defined by the zeroth moment of the distribution functions corrected for the effective source s_{eff} as

$$p = \sum_{i=0}^8 f_i + \frac{\Delta t}{2} s_{\text{eff}}. \quad (15)$$

Since Eq. (14) is purely diffusive, the equilibrium distribution functions are defined by

$$f_i^{\text{eq}} = w_i p. \quad (16)$$

The single-relaxation-time collision step combining Eqs. (10) and (12) then reads

$$f_i^* = f_i - \omega \Delta t (f_i - f_i^{\text{eq}}) + \Delta t S_i, \quad (17)$$

where the contribution by the effective source is given by

$$S_i = \left(1 - \frac{\omega}{2}\right) w_i s_{\text{eff}}. \quad (18)$$

Furthermore, the relaxation rate ω must satisfy $\omega \in (0, 2)$ for stability and is related to the permeability via

$$\kappa = c_s^2 \left(\frac{1}{\omega} - \frac{\Delta t}{2} \right). \quad (19)$$

In the end of each time step, the streaming step of Eq. (11) is performed. Overall, this LBM yields a pressure solution that is second-order consistent in time and space [44].

3.3. The lattice Boltzmann method for quasi-static linear elasticity

Next, we present the necessary steps for the LBM solving the quasi-static linear elasticity Eqs. (5) and (6). The method has been developed in [1, 57] and uses a MRT scheme for the D2Q8 velocity set. For the convenience of the readers, we recapitulate the method in the way it is applied here in the context of Biot's consolidation model. In particular, it solves Eqs. (5) and (6) using an pseudo-timestepping method, where Eq. (5) is replaced by

$$\frac{1}{\varepsilon} \partial_\tau \boldsymbol{\eta} - \nabla \cdot \boldsymbol{\sigma} = \varepsilon \mathbf{f}_{\text{eff}} = \varepsilon (\mathbf{f} - \alpha \nabla p) \quad \text{for } (\tau, t, \mathbf{x}) \in (0, \infty) \times \mathcal{Q}, \quad (20)$$

which is equivalent when the stationary solution is reached (for $\tau \rightarrow \infty$). Note that the division by ε in front of the time derivative is a result of the viscous scaling leading to a pseudo-time step $\Delta\tau = 1$. As before, we defer the computation of the effective force \mathbf{f}_{eff} to Section 3.4.

The moments for the MRT scheme are linear combinations of the raw countable moments [33]

$$m_{ab} = \sum_{i=-1}^1 \sum_{j=-1}^1 i^a j^b g_{ij}, \quad (21)$$

using the two-dimensional Miller index $ab \in \{10, 01, 11, 20, 02, 12, 21, 22\}$, cf. also Table 3 for the inverse transformation. Note that the number of independent moments coincides with the size of the velocity set, i.e., there is no independent zeroth moment $m_{00} = \sum_{i,j} g_{ij}$ due to the absence of the rest velocity \mathbf{c}_{00} . Besides the raw moments m_{ab} with $ab \in \{10, 01, 11, 12, 21\}$, we use the combined second-order moments

$$m_s = m_{20} + m_{02}, \quad m_d = m_{20} - m_{02}, \quad (22)$$

which are directly related to the volumetric and deviatoric components of the stress. Additionally, the raw fourth-order moment m_{22} is replaced by

$$m_f = m_{22} + \frac{1}{12(\lambda + \mu) - 4} m_s, \quad (23)$$

which is required for imposing Neumann boundary conditions [57], see Section 3.5. Here and in the following, we implicitly set the lattice parameter to $\theta = 1/3$ in order to obtain isotropic lattice behavior [1, 57].

Interpreting the LBM as a Strang splitting scheme, the effective force is split into two sub-steps of the collision step [60], and then applied as follows

$$\begin{pmatrix} \bar{m}_{10} \\ \bar{m}_{01} \end{pmatrix} = \begin{pmatrix} m_{10} \\ m_{01} \end{pmatrix} + \frac{\varepsilon^2}{2} \mathbf{f}_{\text{eff}}, \quad \begin{pmatrix} m_{10}^* \\ m_{01}^* \end{pmatrix} = \begin{pmatrix} \bar{m}_{10} \\ \bar{m}_{01} \end{pmatrix} + \frac{\varepsilon^2}{2} \mathbf{f}_{\text{eff}}. \quad (24)$$

Note that this reflects a conservation of the first moments, since no relaxation is applied ($\omega_{10} = \omega_{01} = 0$). All other moments m_ν , $\nu \in \{s, d, 11, 12, 21, f\}$, are relaxed according to the MRT scheme Eq. (13), viz.,

$$m_\nu^* = m_\nu - \omega_\nu (m_\nu - m_\nu^{\text{eq}}), \quad (25)$$

where the relaxation rates ω_ν and equilibrium moments m_ν^{eq} are given in Table 2. In particular, note that the results after half the collision step are denoted by $\bar{m}_\nu = (m_\nu + m_\nu^*)/2$.

Furthermore, the relaxation rates ω_d and ω_{11} are the same (due to the lattice parameter $\theta = 1/3$) in order to obtain isotropic behavior of the deviatoric stress. Indeed, it has been shown in [57] by asymptotic expansion that the displacement $\boldsymbol{\eta}$ and stress $\boldsymbol{\sigma}$ are given in the limit $\tau \rightarrow \infty$ by

$$\boldsymbol{\eta} = \begin{pmatrix} \bar{m}_{10} \\ \bar{m}_{01} \end{pmatrix}, \quad \boldsymbol{\sigma} = -\frac{1}{2} \begin{pmatrix} \bar{m}_s + \bar{m}_d & 2\bar{m}_{11} \\ 2\bar{m}_{11} & \bar{m}_s - \bar{m}_d \end{pmatrix}, \quad (26)$$

Table 2: Relaxation rates ω_ν and equilibrium moments m_ν^{eq} for quasi-static linear elasticity using 2D Miller indices.

Index ν	10	01	s	d	11	12	21	f
Relaxation rate ω_ν	0	0	$2/(3(\lambda + \mu))$	$1/(3\mu)$	$1/(3\mu)$	1	1	1
Equilibrium moment m_ν^{eq}	-	-	0	0	0	$\bar{m}_{10}/3$	$\bar{m}_{01}/3$	0

Table 3: Coefficients c_{ij}^ν of the back-transformation from moments m_ν^* to distribution functions g_{ij}^* using 2D Miller indices, i.e., $\bar{1} = -1$.

$ij \setminus \nu$	01	10	11	s	d	12	21	22
10	$\frac{1}{2}$	0	0	$\frac{1}{4}$	$\frac{1}{4}$	$-\frac{1}{2}$	0	$-\frac{1}{2}$
01	0	$\frac{1}{2}$	0	$\frac{1}{4}$	$-\frac{1}{4}$	0	$-\frac{1}{2}$	$-\frac{1}{2}$
$\bar{1}0$	$-\frac{1}{2}$	0	0	$\frac{1}{4}$	$\frac{1}{4}$	$\frac{1}{2}$	0	$-\frac{1}{2}$
$0\bar{1}$	0	$-\frac{1}{2}$	0	$\frac{1}{4}$	$-\frac{1}{4}$	0	$\frac{1}{2}$	$-\frac{1}{2}$
11	0	0	$\frac{1}{4}$	0	0	$\frac{1}{4}$	$\frac{1}{4}$	$\frac{1}{4}$
$\bar{1}\bar{1}$	0	0	$-\frac{1}{4}$	0	0	$-\frac{1}{4}$	$\frac{1}{4}$	$\frac{1}{4}$
$\bar{1}\bar{1}$	0	0	$\frac{1}{4}$	0	0	$-\frac{1}{4}$	$-\frac{1}{4}$	$\frac{1}{4}$
$1\bar{1}$	0	0	$-\frac{1}{4}$	0	0	$\frac{1}{4}$	$-\frac{1}{4}$	$\frac{1}{4}$

where the involved moments after half the collision can be computed as

$$\bar{m}_s = \frac{3(\lambda + \mu)}{3(\lambda + \mu) + 1} m_s, \quad \bar{m}_d = \frac{6\mu}{6\mu + 1} m_d, \quad \bar{m}_{11} = \frac{6\mu}{6\mu + 1} m_{11}. \quad (27)$$

The post-collision distribution functions are obtained from the back-transformation of the post-collision moments by inverting Eqs. (21) to (23). First, note that this leads to

$$m_{22}^* = -\frac{1}{12(\lambda + \mu) - 4} m_s^* = -\frac{1}{12(\lambda + \mu) + 4} m_s, \quad (28)$$

which is non-singular even for $\lambda + \mu = 1/3$ (alternatively, in this case, the relaxation rate ω_f can be changed without influencing the leading-order behavior [57]). Then, the post-collision distribution functions are given by

$$g_{ij}^* = \sum_\nu c_{ij}^\nu m_\nu^*, \quad (29)$$

where the coefficients c_{ij}^ν are stated in Table 3. In the end of each pseudo-time step, the streaming step of Eq. (11) is performed for the distribution functions g_{ij} . Overall, this LBM yields displacement and stress solutions which are second-order consistent in space for pseudo time $\tau \rightarrow \infty$ (in every time step) [1].

3.4. The coupling of the lattice Boltzmann methods

To obtain the LBM for Biot's consolidation model, we couple the above discussed LBMs for diffuse flow and for quasi-static linear elasticity. To this end, in each time step we solve the quasi-static elasticity problem using $N_E \in \mathbb{N}$ pseudo-time steps, followed by one regular update of the LBM for diffuse flow.

The effective force term $\mathbf{f}_{\text{eff}} = \mathbf{f} - \alpha \nabla p$ in the elasticity Eq. (20) involves the gradient of the pressure. Following [61, 62], this gradient can be approximated up to second-order errors in space by the central difference quotient

$$\nabla^c p(\mathbf{x}) = \sum_{i=1}^8 \frac{w_i \mathbf{c}_i (p(\mathbf{x} + \Delta t \mathbf{c}_i) - p(\mathbf{x} - \Delta t \mathbf{c}_i))}{2c_s^2 \Delta t} = \sum_{i=1}^8 \frac{w_i \mathbf{c}_i p(\mathbf{x} + \Delta t \mathbf{c}_i)}{c_s^2 \Delta t}. \quad (30)$$

However, this requires the pressure defined in Eq. (15), which itself depends on the effective source term $s_{\text{eff}} = s - \kappa \nabla \cdot \mathbf{g} - \frac{\alpha}{\varepsilon} \partial_t^- \nabla \cdot \boldsymbol{\eta}$ in the flow Eq. (14). While the first and second righthand side terms are given explicitly, the last one does depend again on the solution of the elastic equation. To eliminate this cyclic self-dependence, one can use a fully explicit scheme

$$s_{\text{eff}}^{\text{ex}}(t) = s(t) - \kappa \nabla \cdot \mathbf{g}(t) - \frac{\alpha}{\varepsilon} \partial_t^- \nabla \cdot \boldsymbol{\eta}(t - \Delta t) \quad (31)$$

where $\partial_t^- f(t) = (f(t) - f(t - \Delta t))/\Delta t$ denotes the temporal backward difference, while the divergence of the displacement is given according to Eq. (2) by

$$\nabla \cdot \boldsymbol{\eta} = -\bar{m}_s. \quad (32)$$

However, this scheme is unstable for α close to 1, as shown in Section 4.1. Instead, we propose a semi-implicit scheme that utilities the elasticity solution of the previous pseudo-time step, viz.

$$s_{\text{eff}}^{\text{im}}(\tau, t) = s(t) - \kappa \nabla \cdot \mathbf{g}(t) - \frac{\alpha}{\varepsilon} \left((1-r) \partial_t^- \nabla \cdot \boldsymbol{\eta}(t - \Delta t) + r \partial_t^- \nabla \cdot \boldsymbol{\eta}(\tau - \Delta \tau, t) \right), \quad (33)$$

where $r \in [0, 1]$ is the ratio between explicit and semi-implicit approximation. Note that only the rightmost term needs to be recomputed in each pseudo-time step, while the others are computed at the beginning of each time step. Therefore, each time step is initialized by setting $g_{ij}(-1, t) = g_{ij}(0, t) = g_{ij}(N_E, t - \Delta t)$, and after the N_E steps one sets $g_{ij}(t) = g_{ij}(N_E, t)$ and $\nabla \cdot \boldsymbol{\eta}(t) = \nabla \cdot \boldsymbol{\eta}(N_E, t)$. Including the initial and boundary conditions discussed in the following subsection, one obtains Algorithm 1.

Note that an adaptive version of this algorithm using a variable number of pseudo-time steps N_E might be preferential for solutions approaching a stationary state. From an algorithmic point of view, such a change is trivial, as one simply replaces Line 2 by a while loop using the stopping criterion. However from the mathematical theory, it remains unclear, what would be an appropriate stopping criterion. Without known convergence order for the elastic sub-system, a simple criterion using the difference between consecutive iterations could easily fail. Therefore, we restrict ourselves here to the study of the algorithm with fixed number of pseudo-time steps.

Furthermore, with respect to the dimensionless formulation discussed in Section 2.2, note that in the LBM setting one typically chooses the characteristic scales $T \sim \Delta t_{\text{phys}}$ and $L \sim \Delta x_{\text{phys}}$ to obtain step-sizes $\Delta t_{\text{LBM}} = \Delta x_{\text{LBM}} = 1$. Together with a fixed $H \sim 1$, this also yields a small length ratio $\varepsilon \sim \Delta x_{\text{phys}}$ required for the convergence of the LBM for elasticity [1]. Finally, using the viscous scaling $\Delta t_{\text{phys}} \sim (\Delta x_{\text{phys}})^2$ yields constant material parameters, but decreasing forces and source.

3.5. Initial and boundary conditions

Next, we address the LBM implementation of the used initial and boundary conditions. In particular, we discuss periodic, Dirichlet and Neumann boundary conditions for diffuse flow and elasticity. Since all considered domains are axis-aligned and rectangular, we chose the lattice offset to be half of the lattice width, such that it is sufficient to use simple boundary schemes of (anti-)bounce-back type. For more general boundary conditions and complex boundary shapes, we refer to [34, Sec. 8.5] for diffusive flow and [57] for elasticity.

Initial conditions. The initial conditions for all numerical examples given below are

$$p|_{t=0} = 0, \quad \boldsymbol{\eta}|_{t=0} = \mathbf{0}.$$

However, to maintain second-order convergence, the initial conditions in the LBM must be chosen such that the physical initial conditions are satisfied in Eqs. (15) and (26) at $t = 0$ [34, 60]. Hence, the initial distribution functions for pressure and displacement are

$$f_i = -\frac{\Delta t}{2} w_i (s - \kappa \nabla \cdot \mathbf{g})|_{t=0}, \quad g_{ij} = \sum_{\nu} c_{ij}^{\nu} m_{\nu}^0. \quad (34)$$

Algorithm 1 Semi-implicit LBM for poroelasticity.

1:	Set $t = 0$ and initialize the distribution functions f_i and g_{ij}	▷ Eqs. (34) and (35)
2:	for $i = 1, \dots, N_T$ do	
3:	▷ Elasticity update	◁
4:	Set $\tau = 0$ and compute the explicit part of $s_{\text{eff}}^{\text{im}}(t)$	▷ Eq. (33)
5:	for $j = 1, \dots, N_E$ do	
6:	Compute the pressure $p(\tau, t)$ from $s_{\text{eff}}^{\text{im}}(\tau, t)$	▷ Eqs. (15) and (33)
7:	Compute the force $\mathbf{f}_{\text{eff}}(\tau, t)$ from $\nabla p(\tau, t)$	▷ Eqs. (15) and (30)
8:	Compute the moments $m_v(\tau, t)$ from $g_{ij}(\tau, t)$	▷ Eqs. (21) to (23)
9:	Apply half-forcing	▷ Eq. (24)
10:	Compute $\nabla \cdot \boldsymbol{\eta}(\tau, t)$ and the equilibrium moments $m_v^{\text{eq}}(\tau, t)$	▷ Eq. (32) and Table 2
11:	Apply half-forcing	▷ Eq. (24)
12:	Compute the post-collision moments $m_v^*(\tau, t)$	▷ Eq. (25) and Table 2
13:	Back-transform to distributions $g_{ij}^*(\tau, t)$ from $m_v^*(\tau, t)$	▷ Eqs. (28) and (29)
14:	Pseudo-time streaming of the distributions: $g_{ij}(\tau + \Delta\tau, t) = g_{ij}^*(\tau, t)$	
15:	Apply boundary conditions for the linear elasticity	▷ Section 3.5
16:	Advance pseudo time τ by $\Delta\tau$	
17:	Compute $\boldsymbol{\eta}(t)$ and $\boldsymbol{\sigma}(t)$	▷ Eq. (26)
18:	▷ Flow update	◁
19:	Compute the pressure $p(t)$ from $s_{\text{eff}}^{\text{im}}(t)$	▷ Eqs. (15) and (33)
20:	Compute the equilibrium distributions $f_i^{\text{eq}}(t)$	▷ Eq. (16)
21:	Compute the post-collision distributions $f_i^*(t)$	▷ Eqs. (17) and (18)
22:	Streaming of the distributions $f_i(t + \Delta t) = f_i^*(t)$	▷ Eq. (11)
23:	Apply boundary conditions for the pressure	▷ Section 3.5
24:	Advance time t by Δt	

Here, the effective source term at time $t = 0$ disregards the unknown volumetric source $-\frac{\alpha}{\varepsilon} \partial_t \nabla \cdot \boldsymbol{\eta}$. Moreover, the initial moments at time $t = 0$ are the force-corrected equilibrium moments

$$\begin{pmatrix} m_{10}^0 \\ m_{01}^0 \end{pmatrix} = -\frac{\varepsilon^2}{2} \mathbf{f}_{\text{eff}}|_{t=0}, \quad m_s^0 = m_d^0 = m_{11}^0 = 0, \quad \begin{pmatrix} m_{12}^0 \\ m_{21}^0 \end{pmatrix} = -\frac{\varepsilon^2}{6} \mathbf{f}_{\text{eff}}|_{t=0}, \quad m_{22}^0 = 0, \quad (35)$$

where the effective force at time $t = 0$ contains only known terms since $\mathbf{f}_{\text{eff}}|_{t=0} = (\mathbf{f} - \alpha \nabla p)|_{t=0}$. Note that instead of explicitly initializing the distribution functions g_{ij} for elasticity, one could just use more iterations in the first time step to achieve the stationary solution.

Periodic boundary conditions. Periodic boundary conditions on an open and connected subset of the boundary $\Gamma_{\text{per}} \subset \partial \mathcal{D}$ describe solutions repeating indefinitely in space by using the equality of the solution at opposite boundaries of the finite domain $\mathcal{D} = (0, a) \times (0, b)$, $a, b \in \mathbb{R}$, i.e.,

$$p|_{x_1=0} = p|_{x_1=a}, \quad p|_{x_2=0} = p|_{x_2=b}, \quad \boldsymbol{\eta}|_{x_1=0} = \boldsymbol{\eta}|_{x_1=a}, \quad \boldsymbol{\eta}|_{x_2=0} = \boldsymbol{\eta}|_{x_2=b}, \quad \text{on } (0, t_f) \times \Gamma_{\text{per}}.$$

This requires that distribution functions leaving the domain on one side, simultaneously, re-enter at the opposite side. Since the lattice offset is half of the lattice width, this can be realized by simply copying the outgoing distribution functions during streaming to the respective cells on the opposite side. Furthermore, this scheme maintains the convergence order of the underlying LBM. Note that this scheme is automatically included in the streaming step, when a rolling shift implementation is used, e.g., by the function `roll` in the libraries `numpy` or `jax` of Python.

In case of other boundary conditions than periodic ones, there are missing distribution functions after the streaming which would come from outside the domain to the boundary nodes, see Fig. 2 for a sketch at the bottom boundary. These missing distributions can be reconstructed from the post-collision distribution functions taking into account the respective boundary condition. To this end, the basic idea of bounce-back schemes is that distribution functions hitting the boundary are reflected, and thus the missing distributions after streaming are computed from the leaving post-collision distributions in opposite directions.

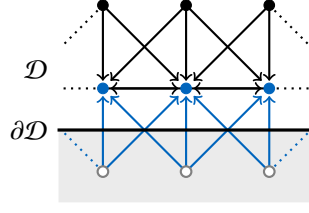


Figure 2: Missing incoming distribution functions (blue) at the bottom boundary of the rectangular domain \mathcal{D} and known incoming distribution functions (black) from inside the domain. Black dots: interior nodes, blue dots: boundary nodes, empty gray nodes: ghost nodes.

Dirichlet boundary conditions. First, we consider a Dirichlet boundary condition for the pressure p to be prescribed on an open and connected subset of the boundary $\Gamma_{D,p} \subset \partial\mathcal{D}$, viz,

$$p = p_D \quad \text{on } (0, t_f) \times \Gamma_{D,p},$$

for some given continuous function $p_D : (0, t_f) \times \Gamma_{D,p} \rightarrow \mathbb{R}$. In this case, we apply the second-order consistent, halfway anti-bounce-back scheme following [42]. When a boundary node with position \mathbf{x} connects via the velocity direction \mathbf{c}_i to the Dirichlet boundary $\Gamma_{D,p}$, then the distribution function at the next time step is given by

$$f_{\check{i}}(t + \Delta t, \mathbf{x}) = -f_i^*(t, \mathbf{x}) + 2w_i p_D(t + \Delta t, \mathbf{x} + \frac{1}{2}\Delta t \mathbf{c}_i). \quad (36)$$

Here, \check{i} denotes the index of the opposite direction of index i , e.g. $\check{4} = 2$ and $\check{5} = 7$, cf. Fig. 1.

Similarly, when a Dirichlet boundary condition for the displacement $\boldsymbol{\eta}$ at an open and connected subset of the boundary $\Gamma_{D,\eta} \subset \partial\mathcal{D}$ is given by

$$\boldsymbol{\eta} = \boldsymbol{\eta}_D \quad \text{on } (0, t_f) \times \Gamma_{D,\eta},$$

for some given continuous function $\boldsymbol{\eta}_D : (0, t_f) \times \Gamma_{D,\eta} \rightarrow \mathbb{R}$, then we use the fullway bounce-back scheme developed in [57]. For a boundary node with position \mathbf{x} connecting to the Dirichlet boundary $\Gamma_{D,\eta}$ via the velocity direction \mathbf{c}_{ij} , the distribution function at the next pseudo-time step is given by

$$g_{\check{i}\check{j}}(\tau + \Delta\tau, t, \mathbf{x}) = g_{ij}(\tau - \Delta\tau, t, \mathbf{x}) - 6w_{ij} \mathbf{c}_{ij} \cdot \boldsymbol{\eta}_D(t, \mathbf{x} + \frac{1}{2}\Delta\tau \mathbf{c}_{ij}). \quad (37)$$

As before, we use the 2D Miller index notation here, i.e., $\bar{1} = -1$, cf. Fig. 1. Note that the delay of one pseudo-time step is equivalent to two full streaming steps into the respective ghost node and back, hence the term “fullway”. Furthermore, this delay is necessary to suppress grid-scale oscillations in the displacement solution according to [57]. As shown therein, this boundary scheme yields a second-order consistent displacement solution and a first-order consistent stress solution for pseudo time $\tau \rightarrow \infty$.

Neumann boundary conditions. For the pressure p , we consider homogeneous Neumann boundary conditions (no-flow conditions) posed on an open and connected subset of the boundary $\Gamma_{N,p} \subset \partial\mathcal{D}$, viz.

$$\kappa \nabla p \cdot \mathbf{n} = 0 \quad \text{on } (0, t_f) \times \Gamma_{N,p},$$

where \mathbf{n} denotes the outward unit normal at the boundary $\Gamma_{N,p}$. This condition can be implemented using the simple halfway bounce-back scheme [34, Sec. 8.5.3]. The new distribution function at a boundary node connecting via the velocity direction \mathbf{c}_i to the Neumann boundary $\Gamma_{N,p}$ is thus given by

$$f_{\check{i}}(t + \Delta t, \mathbf{x}) = f_i^*(t, \mathbf{x}), \quad (38)$$

where \check{i} denotes the opposite direction index introduced above for Dirichlet conditions. Note that this boundary scheme is first-order consistent in general, but second-order consistent if the flux tangential to the boundary vanishes as considered in the numerical example below.

Finally, a Neumann boundary condition (traction condition) can be imposed for the displacement $\boldsymbol{\eta}$ at an open and connected subset of the boundary $\Gamma_{N,\eta} \subset \partial\mathcal{D}$, i.e.,

$$\boldsymbol{\sigma} \mathbf{n} = \mathbf{t} \quad \text{on } (0, t_f) \times \Gamma_{N,\eta},$$

with the outward unit normal \mathbf{n} and some given continuous traction function $\mathbf{t} : (0, t_f) \times \Gamma_{N,\eta} \rightarrow \mathbb{R}^2$. Following [57], we apply a second-order consistent, halfway anti-bounce-back scheme to obtain the missing distribution function at a boundary node connecting via the velocity direction \mathbf{c}_i to the Neumann boundary $\Gamma_{N,\eta}$. This yields

$$g_{i\bar{j}}(\tau + \Delta\tau, t, \mathbf{x}) = -g_{ij}(\tau, t, \mathbf{x}) + \varepsilon \zeta_{i\bar{j}}(t, \mathbf{x} + \frac{1}{2}\Delta t \mathbf{c}_{ij}), \quad (39)$$

where the traction correction terms ζ_{ij} are obtained via the stress Eq. (26) from the traction \mathbf{t} and the normal direction \mathbf{n} . For the left boundary, where $\mathbf{n} = (-1, 0)^\top$, one gets

$$\zeta_{10} = -\sigma_{11} = t_1, \quad \zeta_{11} = -\frac{1}{2}\sigma_{12} = \frac{1}{2}t_2, \quad \zeta_{1\bar{1}} = \frac{1}{2}\sigma_{12} = -\frac{1}{2}t_2.$$

Analogous formulas hold for the right, bottom and top boundaries, but are not explicitly shown here.

4. Numerical Experiments

This section presents several numerical examples to study the numerical accuracy and stability. To this end, we consider three problem settings: the first one is a periodic problem with manufactured solution to assess the performance of the proposed LBM in the bulk without interference of boundary, while the second problem is the two-dimensional version of the classical (quasi-1D) Terzaghi consolidation problem, which even has a discontinuous solution at the initial time due to the instantaneous response to a traction boundary. Finally, the third example extends the latter setting to a truly two-dimensional problem. We present detailed parameter studies concerning the coupling strength, i.e., the Biot–Willis coefficient $\alpha \in (0, 1]$, as well as the convergence with respect to the lattice width Δx and the number of pseudo-time steps N_E , while the time step $\Delta t = \Delta x^2$ follows the typical viscous scaling. Our implementation of the proposed LBM is based on XLB [37], a `jax`-based Python library allowing for parallel LBM simulations. All presented simulations were run on an ordinary workstation with Intel i7-11700 CPU (16 × 2.50GHz).

For the convergence studies, the errors of the numerical solutions of the poroelasticity Eqs. (5) to (8) at the times $t_k = k\Delta t$, $k \in \{0, 1, \dots, N_T\}$, are measured based on the discrete $L^2(\mathcal{D})$ -norm, i.e.,

$$\begin{aligned} e_p^k &= \|p(t_k) - p^{\text{LBM}}(t_k)\|_{L^2(\mathcal{D})} = \Delta x \left(\sum_{m=1}^{N_x N_y} |p(t_k, \mathbf{x}_m) - p^{\text{LBM}}(t_k, \mathbf{x}_m)|^2 \right)^{1/2}, \\ e_\eta^k &= \|\boldsymbol{\eta}(t_k) - \boldsymbol{\eta}^{\text{LBM}}(t_k)\|_{L^2(\mathcal{D})} = \left(\sum_{i=1}^2 \|\eta_i(t_k) - \eta_i^{\text{LBM}}(t_k)\|_{L^2(\mathcal{D})}^2 \right)^{1/2}, \\ e_\sigma^k &= \|\boldsymbol{\sigma}(t_k) - \boldsymbol{\sigma}^{\text{LBM}}(t_k)\|_{L^2(\mathcal{D})} = \left(\sum_{ab \in \{11, 12, 22\}} \|\sigma_{ab}(t_k) - \sigma_{ab}^{\text{LBM}}(t_k)\|_{L^2(\mathcal{D})}^2 \right)^{1/2}, \end{aligned}$$

where N_x and N_y denote the number of lattice cells in x_1 - and x_2 -direction, respectively. Furthermore, the time-space $L^2(\mathcal{Q})$ -error of the pressure is given by

$$e_p = \|p - p^{\text{LBM}}\|_{L^2(\mathcal{Q})} = \Delta t \left(\sum_{k=0}^{N_T} \|e_p^k\|_{L^2(\mathcal{D})}^2 \right)^{1/2},$$

and analogously for the time-space $L^2(\mathcal{Q})$ -error of displacement e_η and of stress e_σ . To have scaling-independent, easily interpretable results, we will primarily report relative errors such as $e_p^{\text{rel}} = e_p / \|p\|_{L^2(\mathcal{Q})}$.

4.1. Periodic problem with manufactured analytical solution

First, a manufactured solution to Eqs. (5) to (8) is considered for numerical validation of accuracy and stability. To avoid the influence of boundary conditions, a periodic problem ($\Gamma_{\text{per}} = \partial\mathcal{D}$) is posed in the domain $\mathcal{D} = (0, 1)^2$ up

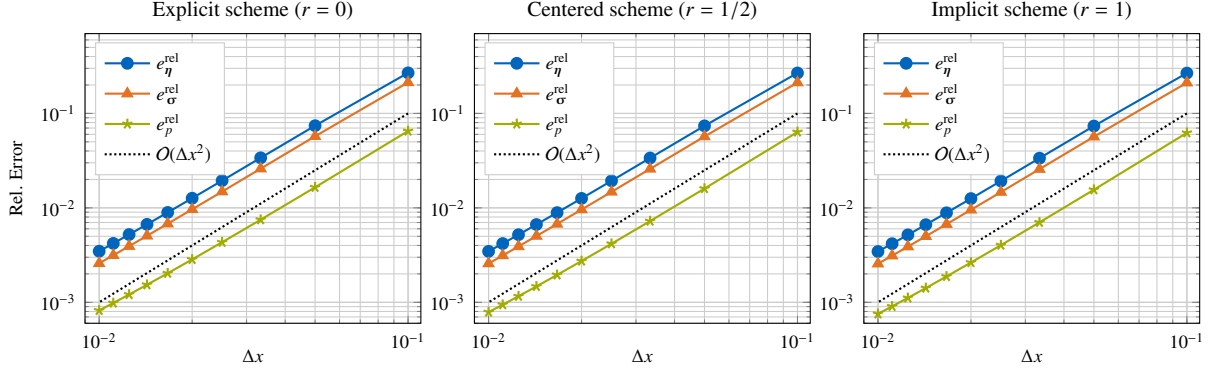


Figure 3: Convergence results for the periodic problem with $\alpha = 0.5$ using $N_E = N_x$ and the explicit, centered and implicit scheme (left to right).

to the final time $t_f = 1$. Inspired by [1], the manufactured solution used here is given by

$$\begin{aligned} \eta(t, \mathbf{x}) &= \frac{1 - \exp(-8\pi^2 kt)}{2} \begin{pmatrix} 9 \cos(2\pi x_1) \sin(2\pi x_2) \\ 7 \sin(2\pi x_1) \cos(2\pi x_2) \end{pmatrix}, \\ p(t, \mathbf{x}) &= -\frac{(16\lambda + 30\mu)\pi}{\alpha} \left(1 - \exp(-8\pi^2 kt)\right) \sin(2\pi x_1) \sin(2\pi x_2), \end{aligned}$$

which leads to the following forces and source term

$$\begin{aligned} \mathbf{f}(t, \mathbf{x}) &= \frac{1 - \exp(-8\pi^2 kt)}{2} \begin{pmatrix} 16\pi^2 \mu \cos(2\pi x_1) \sin(2\pi x_2) \\ 0 \end{pmatrix}, & \mathbf{g}(t, \mathbf{x}) &= \mathbf{0}, \\ s(t, \mathbf{x}) &= -8\pi^3 \kappa \left(16\alpha \exp(-8\pi^2 kt) + \frac{16\lambda + 30\mu}{\alpha}\right) \sin(2\pi x_1) \sin(2\pi x_2). \end{aligned}$$

Setting Young's modulus $E = 0.11$ and Poisson's ratio $\nu = 0.8$ as in [1], the physical parameters are

$$\lambda = \frac{E\nu}{1 - \nu^2} = \frac{11}{45}, \quad \mu = \frac{E}{2(1 + \nu)} = \frac{11}{360}, \quad \kappa = \frac{1}{10},$$

while we consider varying Biot–Willis coefficients $\alpha \in [0.5, 1.0]$. In the following, we discuss the influence of this coefficient α , of the number of pseudo-time steps N_E and of the ratio $r \in \{0, 1/2, 1\}$ in the semi-implicit discretization.

Weak coupling. First, we consider rather low Biot–Willis coefficients $\alpha \leq 0.8$, which means that the poroelastic system is weakly coupled. Furthermore, we fix the number of pseudo-time steps to $N_E = N_x$. This is a compromise between accuracy and run time as the LBM for elasticity needs to approximate the stationary solution ($N_E \rightarrow \infty$) at an algorithmic complexity of $N_E N_x^2$ per time step. In the numerical experiments presented below, we observed that this choice is sufficient because the iteration starts from the solution at the previous time step. Under these conditions, the numerical results indicate almost second-order convergence for decreasing $\varepsilon = \Delta x$, as depicted exemplary for $\alpha = 0.5$ in Fig. 3 and for $\alpha = 0.8$ in Fig. 4. This holds for the explicit scheme with $r = 0$ as well as for the centered scheme ($r = 1/2$) and the implicit one ($r = 1$). In agreement with theory, the errors are the largest for the explicit scheme and lowest for the implicit one. In particular, we observe for all schemes that the errors in the pressure are the smallest, while the relative errors in the stress are smaller than those of the displacement. However, the convergence order for the pressure seems to slightly deteriorate around $\Delta x = 0.01$. This is due to the chosen number of pseudo-time steps $N_E = N_x$. A detailed convergence study for varying N_E is displayed in Fig. 5 for $\alpha = 0.8$ and all three schemes. While the numerical errors are dominated by the elasticity approximation for small N_E as visible by the rather horizontal contour lines, they follow the typical second-order convergence rate for large N_E , where the contour lines are vertically aligned. In particular, the transition between these two regimes seems to occur around $N_E \approx 0.01 N_x^2$, which crosses the above chosen $N_E = N_x$ indeed at $N_x = 100$, i.e., $\Delta x = 0.01$. Besides slightly larger errors for the explicit scheme and slightly smaller ones for the implicit one, there are only very minor differences between the results of all three schemes.

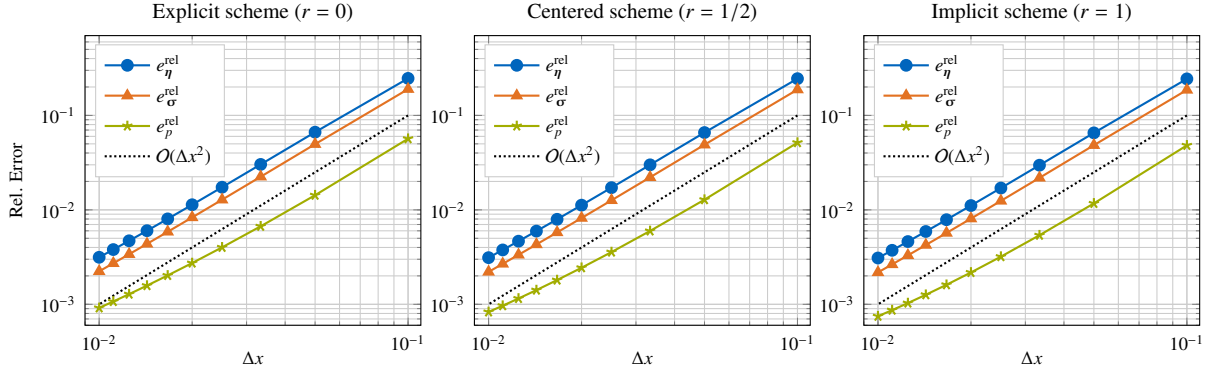


Figure 4: Convergence results for the periodic problem with $\alpha = 0.8$ using $N_E = N_x$ and the explicit, centered and implicit scheme (left to right).

Strong coupling. Next, we consider large Biot–Willis coefficients $\alpha \in \{0.85, 0.9, 1.0\}$, which means that the poroelastic system is strongly coupled. Fixing again $N_E = N_x$, we observe divergence of the errors for both the explicit scheme when $\alpha \geq 0.85$, and for the implicit scheme when $\alpha = 0.9$, as depicted in Fig. 6. Hence, the implicit scheme is slightly better than the explicit one, but ultimately also unstable for α close to 1. Similar behavior has also been observed for other numerical methods due to spurious oscillations between stress and pressure, cf. [18, 23, 24].

On the other hand, the centered scheme still seems to converge at almost second order for all $\alpha \in \{0.85, 0.9, 1.0\}$, see Fig. 6 for $\alpha = 1.0$. Probably, this is due to averaging over two time step which leads to the cancellation of those spurious oscillations. Furthermore, a detailed convergence study for varying N_E is displayed in Fig. 7 for the centered scheme using $\alpha = 1.0$. As for lower α , the elasticity approximation dominates the numerical error below $N_E \approx 0.01N_x^2$, while second-order convergence can be observed above this line. Note that we have observed almost identical results for $\alpha \in \{0.85, 0.9\}$.

4.2. Terzaghi’s consolidation problem

The second poroelastic example originates from Terzaghi’s consolidation problem [9], which describes a fluid-filled soil layer which becomes loaded from above. This leads to a so-called overpressurization of the fluid which continually vanishes due to flow through the surface. Consequently, the elastic soil bears more and more of the the loading and subsides. While the original problem considers the quasi-1D solution to the three-dimensional poroelastic equations ($d = 3$), we adapt the quasi-1D formulation for $d = 2$. Following the derivation in [15, Secs. 5.1 & 5.2.2], we consider Eqs. (5) to (8) in a domain $\mathcal{D} = (0, l) \times (0, 1)$ until the final time $t_f = 1$ with fixed pressure and traction at the top

$$p = 0 \quad \text{and} \quad \boldsymbol{\sigma} \mathbf{n} = \begin{pmatrix} 0 \\ -\varpi \end{pmatrix} \quad \text{on } (0, t_f) \times \{\mathbf{x} \in \partial \mathcal{D} \mid x_2 = 1\},$$

while no-flow condition and fixed displacement are prescribed at the bottom

$$\kappa \nabla p \cdot \mathbf{n} = 0 \quad \text{and} \quad \boldsymbol{\eta} = \mathbf{0} \quad \text{on } (0, t_f) \times \{\mathbf{x} \in \partial \mathcal{D} \mid x_2 = 0\},$$

and periodic boundary conditions are posed on the left and right at $x_1 = 0$ and $x_1 = l$. Note that the length $l > 0$ is irrelevant since the solution is independent of the first spatial coordinate and we choose $l = 4\Delta x$ in the numerical experiments. No external forces or source are present, i.e., $\mathbf{f} \equiv \mathbf{g} \equiv \mathbf{0}$ and $s \equiv 0$. Moreover, the initial conditions are given by

$$p|_{t=0} = 0 \quad \text{and} \quad \boldsymbol{\eta}|_{t=0} = \mathbf{0} \quad \text{in } \mathcal{D}.$$

Due to the incompatibility of the initial and boundary conditions, the solution has a discontinuity at time $t = 0$ with an instantaneous response

$$p(0^+, \mathbf{x}) = p_0 = \frac{\alpha \varpi}{\lambda + 2\mu + \alpha^2} \quad \text{and} \quad \boldsymbol{\eta}(0^+, \mathbf{x}) = \begin{pmatrix} 0 \\ -p_0 x_2 / \alpha \end{pmatrix} \quad \text{for } \mathbf{x} \in \mathcal{D}.$$

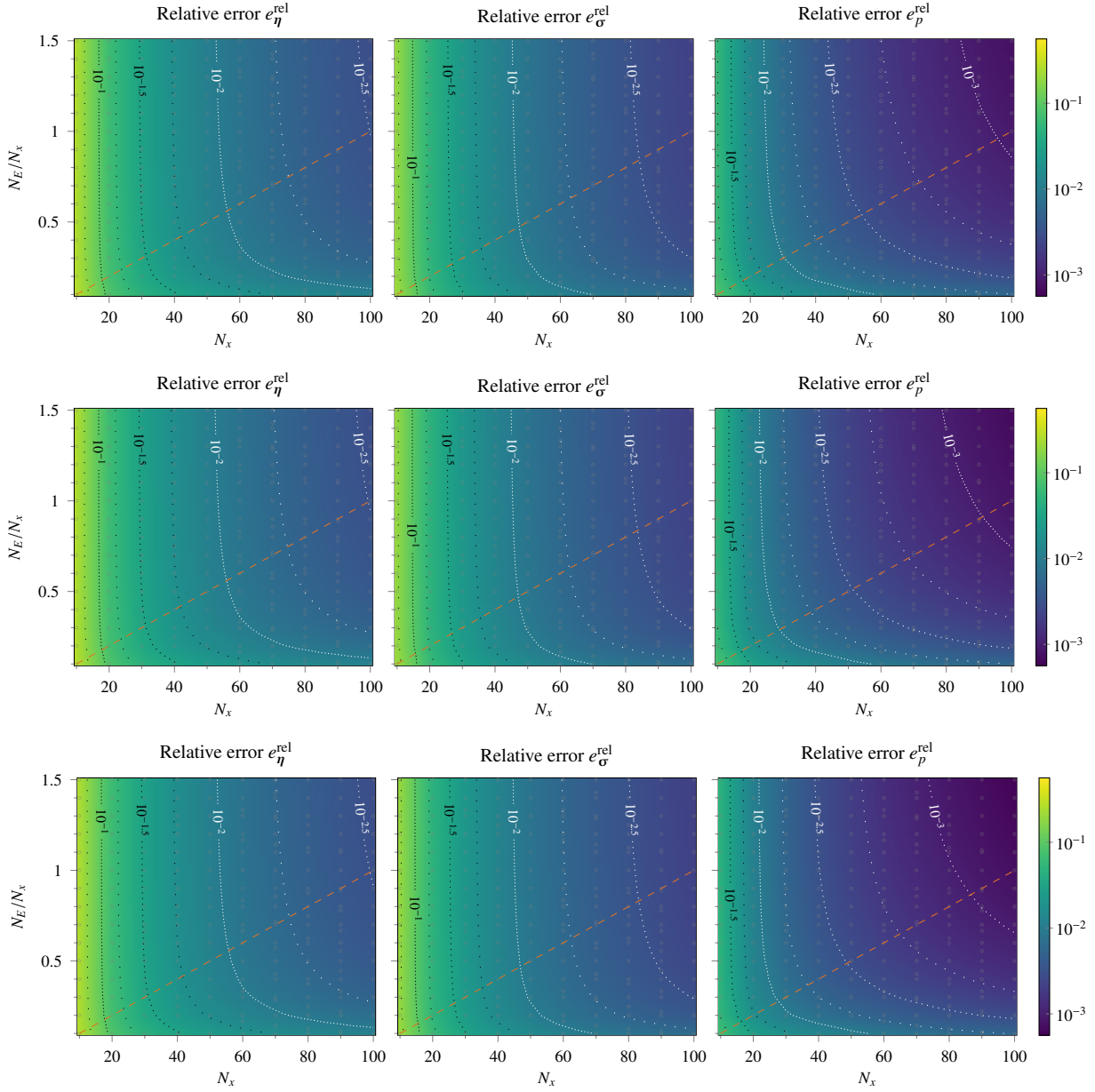


Figure 5: Convergence results for the periodic problem with $\alpha = 0.8$ using the explicit explicit, centered and implicit scheme (top to bottom). The orange dashed line $N_E = 0.01N_x^2$ indicates the transition between dominant error due to discretization of pseudo-timestepping.

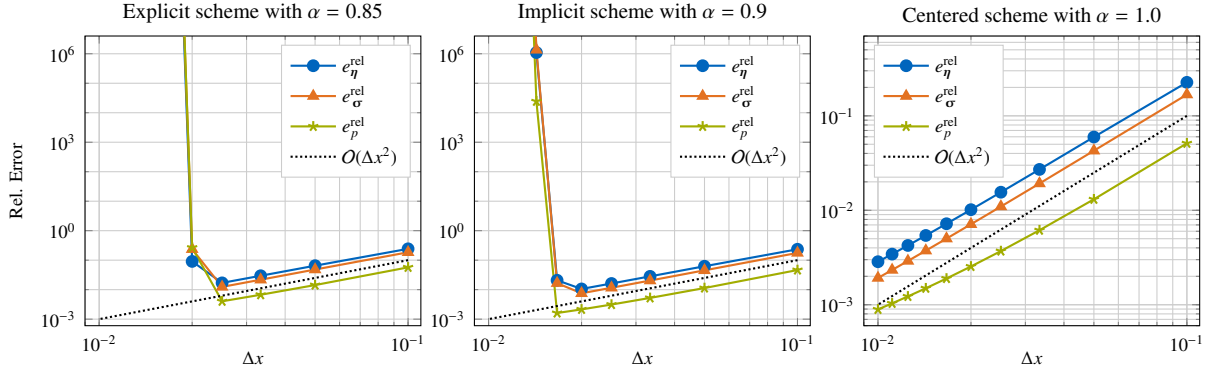


Figure 6: Divergence results for the periodic problem using the explicit scheme ($r = 0$) with $\alpha = 0.85$ (left) and the implicit scheme ($r = 1$) with $\alpha = 0.9$ (center), but convergence of errors for the centered scheme ($r = 1/2$) with $\alpha = 1.0$ (right), using $N_E = N_x$ in all cases.

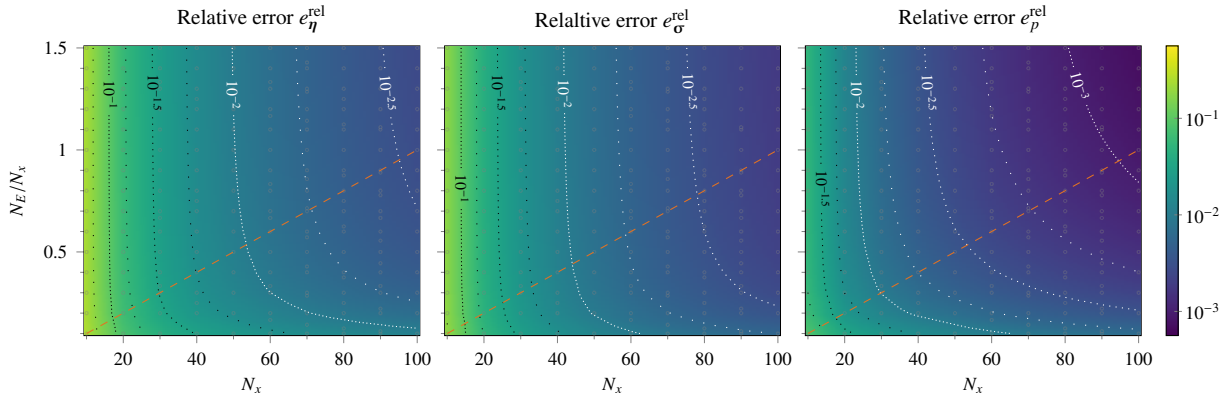


Figure 7: Convergence results for the periodic problem using the centered scheme ($r = 1/2$) for $\alpha = 1.0$. The orange dashed line $N_E = 0.01N_x^2$ indicates the transition between dominant error due to discretization of pseudo-timestepping.

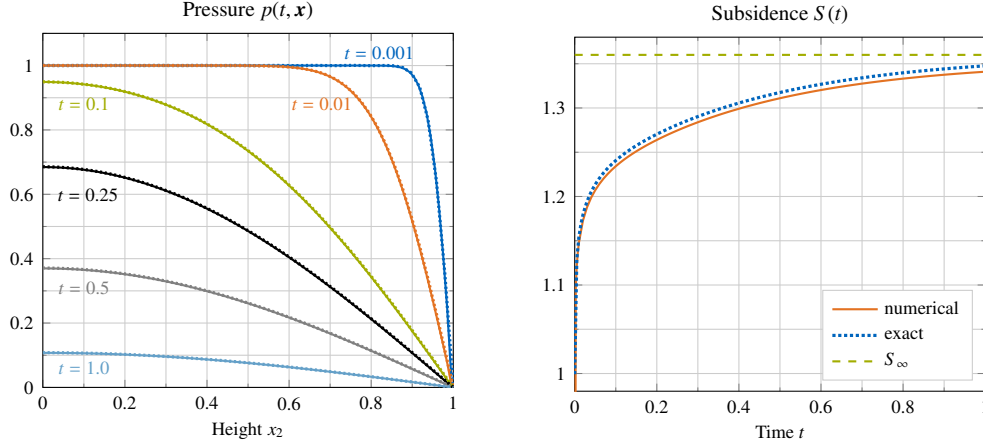


Figure 8: Exact and numerical solutions for Terzaghi's problem with $\alpha = 1.0$ using the centered scheme ($r = 1/2$) with $N_x = 100$ and $N_E = 300$. Dotted lines: exact solution, solid lines: numerical solution.

Hereafter, the solution evolves continuously. In particular, the pressure and the surface subsidence $S = -\eta_2|_{x_2=1}$ are explicitly given by

$$p(t, \mathbf{x}) = p_0 \sum_{k=0}^{\infty} \frac{2(-1)^k}{(k + \frac{1}{2})\pi} \exp\left(-\left(k + \frac{1}{2}\right)^2 \pi^2 c_f t\right) \cos\left(\left(k + \frac{1}{2}\right)\pi x_2\right) \quad \text{for } (t, \mathbf{x}) \in (0, \infty) \times \mathcal{D},$$

$$S(t) = S_{\infty} + (S_0 - S_{\infty}) \sum_{k=0}^{\infty} \frac{2}{(k + \frac{1}{2})^2 \pi^2} \exp\left(-\left(k + \frac{1}{2}\right)^2 \pi^2 c_f t\right) \quad \text{for } t \in (0, \infty),$$

where the effective diffusivity c_f as well as the initial and final surface subsidence are defined as

$$c_f = \frac{\lambda + 2\mu}{\lambda + 2\mu + \alpha^2} \kappa, \quad S_0 = \frac{\varpi}{\lambda + 2\mu + \alpha^2}, \quad S_{\infty} = \frac{\varpi}{\lambda + 2\mu}.$$

Setting Young's modulus $E = 1$ and Poisson's ratio $\nu = 0.8$, we choose the physical parameters

$$\lambda = \frac{E\nu}{1 - \nu^2} = \frac{20}{9}, \quad \mu = \frac{E}{2(1 + \nu)} = \frac{5}{18}, \quad \kappa = \frac{\lambda + 2\mu + \alpha^2}{\lambda + 2\mu} = \frac{25 + 9\alpha^2}{25}, \quad \varpi = \alpha + \frac{\lambda + 2\mu}{\alpha},$$

which implies $p_0 = 1$. Note that due to the permeability $\kappa > 1$, we use a scaling $\Delta t = \Delta x^2/4$ to reduce the numerical errors in the pressure solution. Since only the pressure and the surface subsidence are given analytically, we report relative errors of pressure e_p^{rel} and of subsidence $e_S^{\text{rel}} = \|S - S^{\text{LBM}}\|_{L^2(0,T)} / \|S\|_{L^2(0,T)}$, where the numerical subsidence is defined as average of $-\eta_2$ over the last row of cells next to the boundary at $x_2 = 1$.

The numerical solution of the centered scheme ($r = 1/2$) using $N_E = 3N_x = 300$ and the analytical solution are depicted in detail for $\alpha = 1$ in Fig. 8. The results excellently match already at time $t = 10^{-3}$, thus illustrating that the LBM scheme is well able to reproduce the solution due to instantaneous loading. Fixing again $N_E = 3N_x$, we observe convergence of the centered scheme for varying Biot–Willis coefficient $\alpha \in \{0.8, 0.9, 1.0\}$, as shown in Fig. 9. Due to the discontinuity at time $t = 0$, the convergence order is reduced and seems to lie between 0.5 and 0.75. In contrast to the previous numerical example, also the explicit scheme ($r = 0$) and the implicit scheme ($r = 1$) feature such a convergence behavior for all $\alpha \in \{0.8, 0.9, 1.0\}$. Concerning the influence of the number of pseudo-time steps N_E , a convergence study for the centered scheme ($r = 1/2$) is displayed in Fig. 10 for $\alpha = 1$. Analogously to the periodic example, the numerical errors are dominated by the elasticity approximation for small N_E , while they are dominated by the temporal error for large N_E . Here however, the transition region is wider, and lies around $N_E \approx 0.03N_x^2$. Note that we have observed very similar results for $\alpha \in \{0.8, 0.9\}$ and all three coupling schemes with $r \in \{0, 1/2, 1\}$.

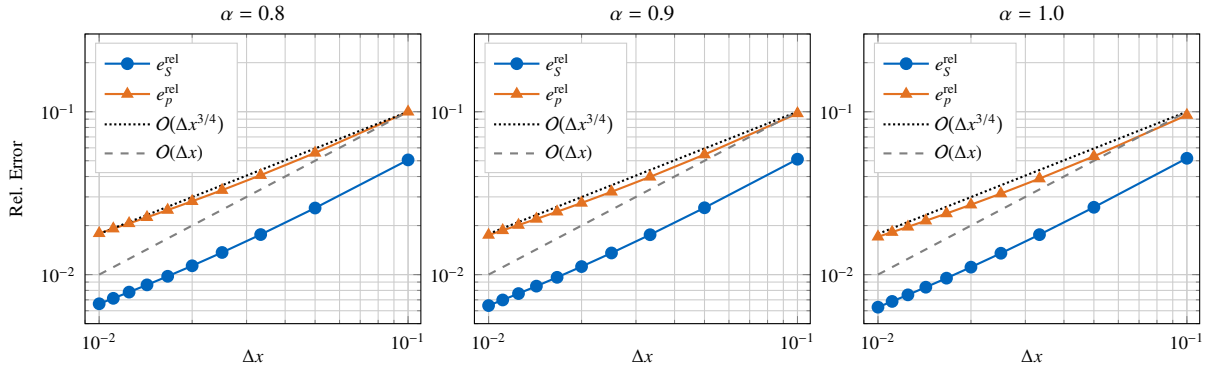


Figure 9: Convergence results for Terzaghi's problem with $\alpha = 0.8, 0.9$ and 1.0 (left to right) using the centered scheme ($r = 1/2$) and $N_E = 3N_x$.

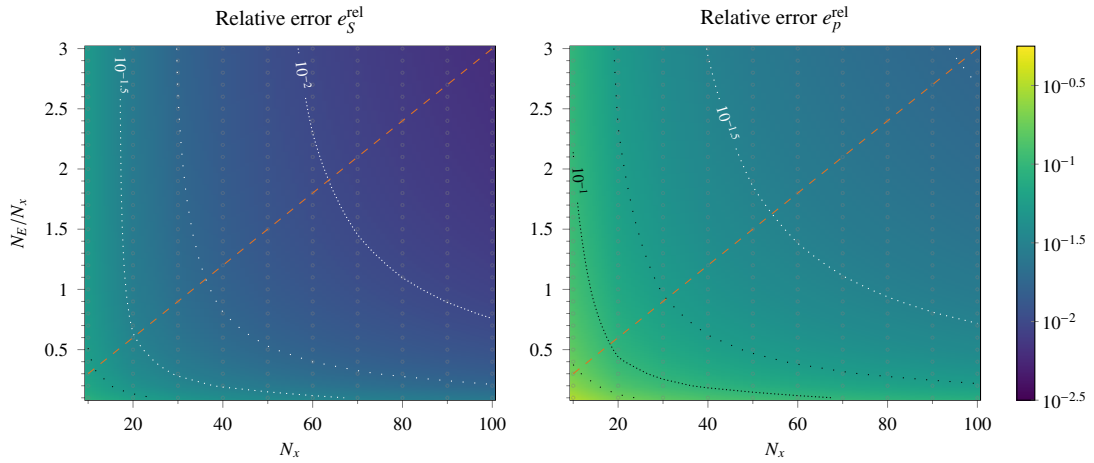


Figure 10: Convergence results for Terzaghi's problem with $\alpha = 1.0$ using the centered scheme ($r = 1/2$). The orange dashed line $N_E = 0.03N_x^2$ indicates the transition between dominant error due to discretization of pseudo-timestepping.

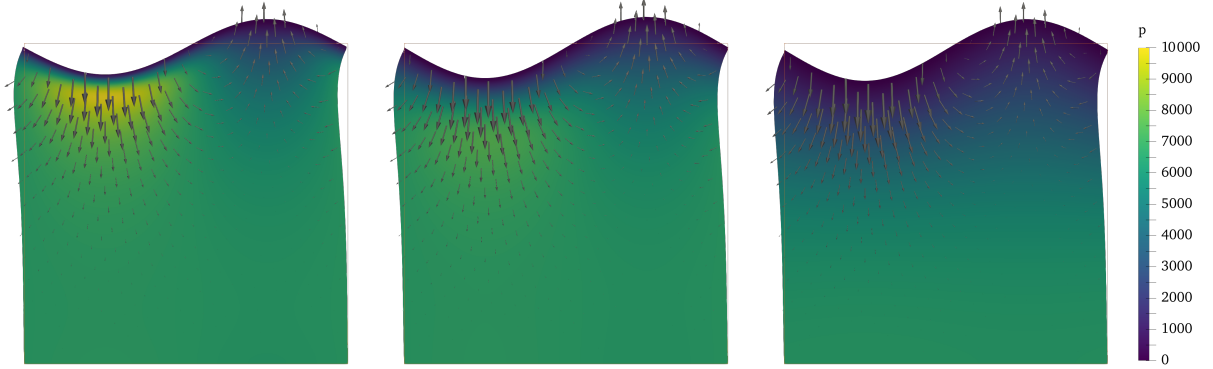


Figure 11: Numerical solutions at the times $t \in \{2 \cdot 10^4, 2 \cdot 10^5, 2 \cdot 10^6\}$ (left to right) for the 2D loading problem using the centered scheme ($r = 1/2$) with $N_x = 100$ and $N_E = 200$. The pressure is represented in color, while the shown displacement is amplified by a factor of 3 and additionally represented by the arrows. The original outline is given by the solid orange line.

4.3. Two-dimensional loading problem

The third example extends Terzaghi's consolidation problem to two dimensions by introducing an position-dependent load. Again, this describes a fluid-filled soil layer which becomes locally loaded from above. The resulting overpressurized fluid slowly flows out through the surface, so that the elastic soil bears more and more of the the loading and subsides. While Terzaghi's problem considers a quasi-1D solution, here we also observe horizontal displacement due to the nonuniform load.

To this end, we consider the dimensional Eqs. (1) to (4) in the domain $\mathcal{D} = (0, 100)^2$ until the final time $t_f = 2 \cdot 10^6$. No external forces or source are present, i.e., $\mathbf{f} \equiv \mathbf{g} \equiv \mathbf{0}$ and $s \equiv 0$, and the initial conditions are

$$p|_{t=0} = 0 \quad \text{and} \quad \boldsymbol{\eta}|_{t=0} = \mathbf{0} \quad \text{in } \mathcal{D}.$$

At the top boundary, pressure and traction are imposed

$$p = 0 \quad \text{and} \quad \boldsymbol{\sigma} \mathbf{n} = \begin{pmatrix} 0 \\ -10^4 \left(1 - \cos\left(\frac{x_1 + 25}{50} \pi\right)\right) \end{pmatrix} \quad \text{on } (0, t_f) \times \{\mathbf{x} \in \partial\mathcal{D} \mid x_2 = 100\},$$

whereas no-flow condition and fixed displacement are given at the bottom

$$\kappa \nabla p \cdot \mathbf{n} = 0 \quad \text{and} \quad \boldsymbol{\eta} = \mathbf{0} \quad \text{on } (0, t_f) \times \{\mathbf{x} \in \partial\mathcal{D} \mid x_2 = 0\}.$$

Furthermore, periodic boundary conditions are prescribed on the left and right boundaries at $x_1 \in \{0, 100\}$. Setting Young's modulus $E = 10^5$ and Poisson's ratio $\nu = 0.9$, we choose the physical parameters

$$\lambda = \frac{E\nu}{1 - \nu^2} = \frac{9 \cdot 10^6}{19}, \quad \mu = \frac{E}{2(1 + \nu)} = \frac{5 \cdot 10^5}{19}, \quad c_0 = 10^{-6}, \quad \kappa = 10^{-9},$$

and consider the strongly coupled situation where $\alpha = 1$. Note that the incompatibility of the initial and boundary conditions again yields a solution which is discontinuous at time $t = 0$.

The numerical solution of the centered scheme ($r = 1/2$) using $N_E = 2N_x = 200$ and $N_T = 10^4$ is depicted at the times $t \in \{2 \cdot 10^4, 2 \cdot 10^5, 2 \cdot 10^6\}$ in Fig. 11. Since the load is concentrated on the left half, the subsidence is significant there, while the surface on the right is even lifted. Furthermore, this leads to a horizontal expansion from the left half to the right one. In the beginning, the fluid pressure is very large close to the left half of the surface, while it is low on the right half. As expected, the pressure slowly vanishes over time resulting in a further subsidence of the whole surface.

5. Conclusion

In this work, we developed a novel coupling of LBMs to solve Biot’s consolidation model in two dimensions. To this end, we combined the classical LBM for reaction-diffusion equations [44] with the recent pseudo-time LBM for quasi-static linear elasticity [1]. Therefore, the overall method uses only two distribution functions with (reduced) standard velocity sets for the solution fields, so that 17 unknowns per cell are required to solve for the 6 components of pressure, displacement and stress field at second-order consistency.

Numerical results obtained with the method of manufactured solutions confirm the analytical properties of the coupled methods. This concerns the second-order convergence wrt. time-step size and lattice width for a quadratic number of pseudo-time steps $N_E \sim N_x^2$. The latter is due to the explicit pseudo-timestepping inherent to the LBM for quasi-static elasticity. We have demonstrated that naively coupled LBMs lead to instabilities for strong coupling with Biot–Willis coefficient α close to 1, as both the fully explicit scheme and the semi-implicit scheme yield diverging solutions. However, the centered coupling scheme, which uses half of both contributions (fully explicit and semi-implicit), is stable and accurate for all Biot–Willis coefficients. Moreover, the presented numerical results for Terzaghi’s (quasi-1D) consolidation problem and for a two-dimensional expansion thereof, both incorporate an instantaneous response due to external loading, and hence demonstrate that the coupled LBM is even applicable to discontinuous problems.

The main drawback of the method lies in its pseudo-timestepping for quasi-static elasticity, which results in an algorithmic complexity of $O(N_x^6)$. However, the small prefactor observed in numerical experiments partially remedies this shortcoming. Furthermore, an adaptive choice of N_E depending on a convergence criterion such as the difference between consecutive pseudo-time steps might further reduce the computational cost.

On the other hand, the method has several advantages, as it allows for a simple and scalable parallelization and is second-order consistent in space and time for all three solution fields.

In view of the fact, that this is the initial application of LBM to poroelasticity, there are ample opportunities for further development. Besides possible extensions to three-dimensional and nonlinear poroelastic equations, different LBMs might be used to solve the flow and/or elasticity subproblems. In particular, solving the flow equations by a MRT scheme like in [42] could allow for anisotropic permeability, while accounting for elastodynamics solved by LBMs as e.g. in [51, 55] would enable the study of seismic waves in aquifers and reservoirs.

CRedit authorship contribution statement

Stephan B. Lunowa: Conceptualization, Data curation, Formal analysis, Investigation, Methodology, Software, Validation, Visualization, Writing – original draft, Writing – review and editing. **Barbara Wohlmuth:** Conceptualization, Funding acquisition, Methodology, Resources, Supervision, Writing – review and editing.

Declaration of competing interest

The authors declare that they have no known competing financial interests or personal relationships that could have appeared to influence the work reported in this paper.

Data availability

The codes required to reproduce the above findings will be made available on request.

References

- [1] O. Boolakee, M. Geier, L. De Lorenzis, A new lattice Boltzmann scheme for linear elastic solids: periodic problems, *Comput. Methods Appl. Mech. Engrg.* 404 (2023) 115756. doi:10.1016/j.cma.2022.115756.
- [2] J. M. Nordbotten, M. A. Celia, *Geological Storage of CO₂: Modeling Approaches for Large-Scale Simulation*, Wiley, 2011. doi:10.1002/9781118137086.
- [3] T. Sharmin, N. R. Khan, M. S. Akram, M. M. Ehsan, A state-of-the-art review on geothermal energy extraction, utilization, and improvement strategies: conventional, hybridized, and enhanced geothermal systems, *Internat. J. Thermofluids* 18 (2023) 100323. doi:10.1016/j.ijft.2023.100323.

- [4] H. Alkhatib, A. Al-Ostaz, A. H.-D. Cheng, X. Li, Materials genome for graphene-cement nanocomposites, *J. Nanomech. Micromech.* 3 (3) (2013) 67–77. doi:10.1061/(ASCE)NM.2153-5477.0000055.
- [5] M. Vandamme, F.-J. Ulm, Nanoindentation investigation of creep properties of calcium silicate hydrates, *Cem. Concr. Res.* 52 (2013) 38–52. doi:10.1016/j.cemconres.2013.05.006.
- [6] A.-R. A. Khaled, K. Vafai, The role of porous media in modeling flow and heat transfer in biological tissues, *Internat. J. Heat Mass Transfer* 46 (26) (2003) 4989–5003. doi:10.1016/S0017-9310(03)00301-6.
- [7] P. Causin, G. Guidoboni, A. Harris, D. Prada, R. Sacco, S. Terragni, A poroelastic model for the perfusion of the lamina cribrosa in the optic nerve head, *Math.l Biosci.* 257 (2014) 33–41. doi:10.1016/j.mbs.2014.08.002.
- [8] D. Chapelle, J.-F. Gerbeau, J. Sainte-Marie, I. E. Vignon-Clementel, A poroelastic model valid in large strains with applications to perfusion in cardiac modeling, *Comput. Mech.* 46 (2010) 91–101. doi:10.1007/s00466-009-0452-x.
- [9] K. Terzaghi, Die Berechnung der Durchlässigkeitsziffer des Tones aus dem Verlauf der hydrodynamischen Spannungsercheinungen, *Sitzungsberichte Akademie der Wissenschaften, Wien Mathematisch-Naturwissenschaftliche Klasse, Abteilung IIa* 132 (1923) 105–124.
- [10] M. A. Biot, Consolidation settlement under a rectangular load distribution, *J. Appl. Phys.* 12 (5) (1941) 426–430. doi:10.1063/1.1712921.
- [11] M. A. Biot, General theory of three-dimensional consolidation, *J. Appl. Phys.* 12 (2) (1941) 155–164. doi:10.1063/1.1712886.
- [12] M. A. Biot, Theory of elasticity and consolidation for a porous anisotropic solid, *J. Appl. Phys.* 26 (2) (1955) 182–185. doi:10.1063/1.1721956.
- [13] M. A. Biot, D. G. Willis, The elastic coefficients of the theory of consolidation, *J. Appl. Mech.* 15 (1957) 594–601. doi:10.1115/1.4011606.
- [14] E. Detournay, A. H.-D. Cheng, Fundamentals of poroelasticity, in: C. Fairhurst (Ed.), *Analysis and Design Methods*, Pergamon, 1993, pp. 113–171. doi:10.1016/B978-0-08-040615-2.50011-3.
- [15] O. Coussy, *Poromechanics*, Wiley, 2004. doi:10.1002/0470092718.
- [16] G. N. Mercer, S. I. Barry, Flow and deformation in poroelasticity – II Numerical method, *Math. Comput. Model.* 30 (9) (1999) 31–38. doi:10.1016/S0895-7177(99)00178-8.
- [17] F. J. Gaspar, F. J. Lisbona, P. N. Vabishchevich, Finite difference schemes for poro-elastic problems, *Comput. Meth. Appl. Math.* 2 (2) (2002) 132–142. doi:10.2478/cmam-2002-0008.
- [18] M. Bean, S.-Y. Yi, An immersed interface method for a 1D poroelasticity problem with discontinuous coefficients, *J. Comput. Appl. Math.* 272 (2014) 81–96. doi:10.1016/j.cam.2014.05.009.
- [19] R. W. Lewis, B. A. Schrefler, *The Finite Element Method in the Deformation and Consolidation of Porous Media*, Wiley, 1987.
- [20] M. A. Murad, A. F. D. Loula, On stability and convergence of finite element approximations of Biot’s consolidation problem, *Internat. J. Numer. Meth. Engrg.* 37 (4) (1994) 645–667. doi:10.1002/nme.1620370407.
- [21] J. M. Nordbotten, Stable cell-centered finite volume discretization for Biot equations, *SIAM J. Numer. Anal.* 54 (2) (2016) 942–968. doi:10.1137/15M1014280.
- [22] I. Sokolova, M. G. Bastisa, H. Hajibeygi, Multiscale finite volume method for finite-volume-based simulation of poroelasticity, *J. Comput. Phys.* 379 (2019) 309–324. doi:10.1016/j.jcp.2018.11.039.
- [23] K. M. Terekhov, Cell-centered finite-volume method for heterogeneous anisotropic poromechanics problem, *J. Comput. Appl. Math.* 365 (2020) 112357. doi:10.1016/j.cam.2019.112357.
- [24] P. J. Phillips, M. F. Wheeler, A coupling of mixed and discontinuous Galerkin finite-element methods for poroelasticity, *Comput. Geosci.* 12 (2008) 417–435. doi:10.1007/s10596-008-9082-1.
- [25] R. Liu, M. F. Wheeler, C. N. Dawson, R. H. Dean, On a coupled discontinuous/continuous Galerkin framework and an adaptive penalty scheme for poroelasticity problems, *Comput. Meth. Appl. Mech. Engrg.* 198 (41) (2009) 3499–3510. doi:10.1016/j.cma.2009.07.005.
- [26] M. Wheeler, G. Xue, I. Yotov, Coupling multipoint flux mixed finite element methods with continuous Galerkin methods for poroelasticity, *Comput. Geosci.* 18 (2014) 57–75. doi:10.1007/s10596-013-9382-y.
- [27] I. Ambartsumyan, E. Khattatov, I. Yotov, A coupled multipoint stress–multipoint flux mixed finite element method for the Biot system of poroelasticity, *Comput. Meth. Appl. Mech. Engrg.* 372 (2020) 113407. doi:10.1016/j.cma.2020.113407.
- [28] J. Choo, S. Lee, Enriched Galerkin finite elements for coupled poromechanics with local mass conservation, *Comput. Meth. Appl. Mech. Engrg.* 341 (2018) 311–332. doi:10.1016/j.cma.2018.06.022.
- [29] G. R. McNamara, G. Zanetti, Use of the Boltzmann equation to simulate lattice-gas automata, *Phys. Rev. Lett.* 61 (1988) 2332–2335. doi:10.1103/PhysRevLett.61.2332.
- [30] S. Chen, G. D. Doolen, Lattice Boltzmann method for fluid flows, *Annu. Rev. Fluid Mech.* 30 (1998) 329–364. doi:10.1146/annurev.fluid.30.1.329.
- [31] P. L. Bhatnagar, E. P. Gross, M. Krook, A model for collision processes in gases. I. Small amplitude processes in charged and neutral one-component systems, *Phys. Rev.* 94 (1954) 511–525. doi:10.1103/PhysRev.94.511.
- [32] D. d’Humières, Multiple-relaxation-time lattice Boltzmann models in three dimensions, *Phil. Trans. R. Soc. A.* 360 (2002) 437–451. doi:10.1098/rsta.2001.0955.
- [33] M. Geier, M. Schönherr, A. Pasquali, M. Krafczyk, The cumulant lattice Boltzmann equation in three dimensions: Theory and validation, *Comput. Math. Appl.* 70 (4) (2015) 507–547. doi:10.1016/j.camwa.2015.05.001.
- [34] T. Krüger, H. Kusumaatmaja, A. Kuzmin, O. Shardt, G. Silva, E. M. Viggen, *The Lattice Boltzmann Method*, Springer, 2017. doi:10.1007/978-3-319-44649-3.
- [35] S. Succi, *The Lattice Boltzmann Equation: For Complex States of Flowing Matter*, Oxford University Press, 2018. doi:10.1093/oso/9780199592357.001.0001.
- [36] M. Schönherr, K. Kucher, M. Geier, M. Stiebler, S. Freudiger, M. Krafczyk, Multi-thread implementations of the lattice Boltzmann method on non-uniform grids for CPUs and GPUs, *Comput. Math. Appl.* 61 (12) (2011) 3730–3743. doi:10.1016/j.camwa.2011.04.012.
- [37] M. Ataei, H. Salehipour, XLB: A differentiable massively parallel lattice Boltzmann library in Python, *Comput. Phys. Commun.* 300 (2024) 109187. doi:10.1016/j.cpc.2024.109187.
- [38] D. Wolf-Gladrow, A lattice Boltzmann equation for diffusion, *J. Stat. Phys.* 79 (1995) 1023–1032. doi:10.1007/BF02181215.

- [39] E. G. Flekkøy, Lattice Bhatnagar-Gross-Krook models for miscible fluids, *Phys. Rev. E* 47 (1993) 4247–4257. doi:10.1103/PhysRevE.47.4247.
- [40] S. Ponce Dawson, S. Chen, G. D. Doolen, Lattice Boltzmann computations for reaction-diffusion equations, *J. Chem. Phys.* 98 (2) (1993) 1514–1523. doi:10.1063/1.464316.
- [41] X. Zhang, A. G. Bengough, J. W. Crawford, I. M. Young, A lattice BGK model for advection and anisotropic dispersion equation, *Adv. Water Resour.* 25 (1) (2002) 1–8. doi:10.1016/S0309-1708(01)00047-1.
- [42] I. Ginzburg, Equilibrium-type and link-type lattice Boltzmann models for generic advection and anisotropic-dispersion equation, *Adv. Water Resour.* 28 (11) (2005) 1171–1195. doi:10.1016/j.advwatres.2005.03.004.
- [43] B. Shi, B. Deng, R. Du, X. Chen, A new scheme for source term in LBGK model for convection–diffusion equation, *Comput. Math. Appl.* 55 (7) (2008) 1568–1575. doi:10.1016/j.camwa.2007.08.016.
- [44] T. Seta, Implicit temperature-correction-based immersed-boundary thermal lattice Boltzmann method for the simulation of natural convection, *Phys. Rev. E* 87 (2013) 063304. doi:10.1103/PhysRevE.87.063304.
- [45] Q. Li, Z. Chai, B. Shi, Lattice Boltzmann model for a class of convection–diffusion equations with variable coefficients, *Comput. Math. Appl.* 70 (4) (2015) 548–561. doi:10.1016/j.camwa.2015.05.008.
- [46] Z. Chai, B. Shi, Z. Guo, A multiple-relaxation-time lattice Boltzmann model for general nonlinear anisotropic convection-diffusion equations, *J. Sci. Comput.* 69 (2016) 355–390. doi:10.1007/s10915-016-0198-5.
- [47] Z. Chai, B. Shi, Multiple-relaxation-time lattice Boltzmann method for the Navier-Stokes and nonlinear convection-diffusion equations: Modeling, analysis, and elements, *Phys. Rev. E* 102 (2020) 023306. doi:10.1103/PhysRevE.102.023306.
- [48] S. Marconi, B. Chopard, A lattice Boltzmann model for a solid body, *Internat. J. Modern Phys. B* 17 (1–2) (2003) 153–156. doi:10.1142/S0217979203017254.
- [49] G. S. O’Brien, T. Nissen-Meyer, C. J. Bean, A lattice Boltzmann method for elastic wave propagation in a Poisson solid, *Bull. Seismol. Soc. Am.* 102 (3) (2012) 1224–1234. doi:10.1785/0120110191.
- [50] J. S. N. Murthy, P. K. Kolluru, V. Kumaran, S. Ansumali, Lattice Boltzmann method for wave propagation in elastic solids, *Commun. Comput. Phys.* 23 (4) (2018) 1223–1240. doi:10.4208/cicp.OA-2016-0259.
- [51] M. Escande, P. K. Kolluru, L. M. Cléon, P. Sagaut, Lattice Boltzmann method for wave propagation in elastic solids with a regular lattice: Theoretical analysis and validation (2020). arXiv:2009.06404.
- [52] E. Faust, A. Schlüter, H. Müller, F. Steinmetz, R. Müller, Dirichlet and Neumann boundary conditions in a lattice Boltzmann method for elastodynamics, *Comput. Mech.* 73 (2024) 317–339. doi:10.1007/s00466-023-02369-w.
- [53] A. Schlüter, C. Kuhn, R. Müller, Lattice Boltzmann simulation of antiplane shear loading of a stationary crack, *Comput. Mech.* 62 (2018) 1059–1069. doi:10.1007/s00466-018-1550-4.
- [54] A. Schlüter, H. Müller, R. Müller, Boundary conditions in a lattice Boltzmann method for plane strain problems, *PAMM* 21 (1) (2021) e202100085. doi:10.1002/pamm.202100085.
- [55] O. Boolakee, M. Geier, L. De Lorenzis, Lattice Boltzmann for linear elastodynamics: periodic problems and Dirichlet boundary conditions (2024). arXiv:2408.01081.
- [56] X. Yin, G. Yan, T. Li, Direct simulations of the linear elastic displacements field based on a lattice Boltzmann model, *Internat. J. Numer. Meth. Engrg.* 107 (3) (2016) 234–251. doi:https://doi.org/10.1002/nme.5167.
- [57] O. Boolakee, M. Geier, L. De Lorenzis, Dirichlet and Neumann boundary conditions for a lattice Boltzmann scheme for linear elastic solids on arbitrary domains, *Comput. Methods Appl. Mech. Engrg.* 415 (2023) 116225. doi:10.1016/j.cma.2023.116225.
- [58] J.-L. Auriault, E. Sanchez-Palencia, Etude du comportement macroscopique d’un milieu poreux saturé déformable, *J. Mécanique* 16 (4) (1977) 575–603.
- [59] R. E. Showalter, Diffusion in poro-elastic media, *J. Math. Anal. Appl.* 251 (1) (2000) 310–340. doi:10.1006/jmaa.2000.7048.
- [60] P. J. Dellar, An interpretation and derivation of the lattice Boltzmann method using Strang splitting, *Comput. Math. Appl.* 65 (2) (2013) 129–141. doi:10.1016/j.camwa.2011.08.047.
- [61] T. Lee, C.-L. Lin, A stable discretization of the lattice Boltzmann equation for simulation of incompressible two-phase flows at high density ratio, *J. Comput. Phys.* 206 (1) (2005) 16–47. doi:10.1016/j.jcp.2004.12.001.
- [62] T. Lee, P. F. Fischer, Eliminating parasitic currents in the lattice Boltzmann equation method for nonideal gases, *Phys. Rev. E* 74 (2006) 046709. doi:10.1103/PhysRevE.74.046709.